Diffuse Optical Tomography of Highly Heterogeneous Media

Vasilis Ntziachristos*, Andreas H. Hielscher, A. G. Yodh, and Britton Chance

***Abstract*—We investigate the performance of diffuse optical tomography to image highly heterogeneous media, such as breast tissue, as a function of background heterogeneity. To model the background heterogeneity, we have employed the functional information derived from Gadolinium-enhanced magnetic resonance images of the breast. We demonstrate that overall image quality and quantification accuracy worsens as the background heterogeneity increases. Furthermore we confirm the appearance of characteristic artifacts at the boundaries that scale with background heterogeneity. These artifacts are very similar to the ones seen in clinical examinations and can be misinterpreted as actual objects if not accounted for. To eliminate the artifacts and improve the overall image reconstruction, we apply a data-correction algorithm that yields superior reconstruction results and is virtually independent of the degree of the background heterogeneity.**

***Index Terms*—Artifacts, correction, diffuse media, diffuse optical tomography, reconstruction.**

I. Introduction

THE theoretical and technological advances accomplished over the last decade in the field of the near-infrared (NIR) diffuse optical tomography (DOT) has led to the development of imaging devices aiming at investigating the clinical capacity of the technique [1]–[3]. Human breast cancer diagnosis is a major target for these imagers, since the disease is a leading cause of death among women in North America and Europe. DOT offers the potential for three-dimensional (3-D) imaging and quantification of tissue chromophores such as oxy- and deoxy-hemoglobin, of contrast agents and of tissue scattering. Tomography of fluorescence, or of absorption and scattering at multiple wavelengths, can yield images of tissue hemoglobin concentration and oxygen saturation after appropriate spectral processing [4], of contrast agent uptake and release, and of organelle concentration [5]. The revealed tissue functional characteristics may lead to the study of cancers and increase diagnostic specificity.

Manuscript received June 2, 2000; revised March 28, 2001. This work was supported by the National Institutes of Health (NIH) under Grant ROI CA60182. The Associate Editor responsible for coordinating the review of this paper and recommending its publication was R. Barbour. *Asterisk indicates corresponding author.*

*V. Ntziachristos is with the Department of Bioengineering and the Department of Biochemistry/Biophysics, University of Pennsylvania, Philadelphia, PA 19104 USA, and also with the Center for Molecular Imaging Research, Massachusetts General Hospital and Harvard Medical School, Building 149, 13th Street 5406, Charlestown, MA 02129-2060 USA (e-mail: vasilis@helix.mgh.harvard.edu).

A. H. Hielscher is with the Department of Pathology, State University of New York, Health Science Center, Brooklyn, NY 11201 USA.

A. G. Yodh is with the Department of Physics and Astronomy, University of Pennsylvania, Philadelphia, PA 19104 USA.

B. Chance is with the Department of Biochemistry/Biophysics, University of Pennsylvania, Philadelphia, PA 19104 USA.

Publisher Item Identifier S 0278-0062(01)04692-4.

The capability of DOT to resolve objects embedded in otherwise homogeneous media has been studied in the past with simulated and experimental data. The technique is generally of low resolution but offers high localization ability and quantification accuracy in the range of 10% to 50% depending on the geometry employed, the signal to noise and the inversion technique used.

As DOT moves toward clinical applications, it becomes critical to evaluate its image fidelity within highly heterogeneous, tissue-like media. In the past, segmentation of T_1-weighted magnetic resonance (MR) images of the brain and breast has been employed to produce maps of optical heterogeneity [6], [7]. In these studies, the segmentation of the MR images assumed that the variation of tissue optical properties coincided with tissue anatomy. The study by Chang *et al.* [6] found that in the absence of *a priori* knowledge of the background heterogeneity, DOT is unable to resolve objects simulating pathologies. Pogue *et al.* [7] demonstrated that heterogeneity distribution cannot be reconstructed accurately without using *a priori* information.

The objective of this paper was: 1) to systematically study the effect of breast-like optical heterogeneity on DOT performance; 2) to evince on the appearance of characteristic artifacts in front of the sources and detectors because of this heterogeneity; and 3) to show that under certain practical conditions a proposed data normalization algorithm can be used to significantly improve the reconstruction performance in the absence of *a priori* image information. We have used a finite-difference solver [8] of the heterogeneous diffusion equation in the time domain to obtain forward data and a perturbative solution of the heterogeneous diffusion equation for data inversion. In contrast to previous studies, the modeling of optical heterogeneity was based on a segmentation method that used the breast vasculature pattern to simulate tissue-like maps, as this may be more representative of the breast optical contrast.

The results indicate that the emergence of artifacts scales with background heterogeneity and may lead to erroneous misinterpretation of the reconstructed images. Such artifacts have been seen in our simultaneous examinations of the breast with MR Imaging and DOT [9]. Here, we can systematically establish our initial hypothesis that such artifacts are due to the background heterogeneity. The reconstruction of localized lesions simulating pathologies also deteriorates as a function of background heterogeneity. We find that increasing the data set size, specifically the number of detectors used, improves the reconstruction of the tumor structure but it does not remove the artifacts. We further demonstrate that the correction algorithm employed not only improves the reconstruction but also eliminates

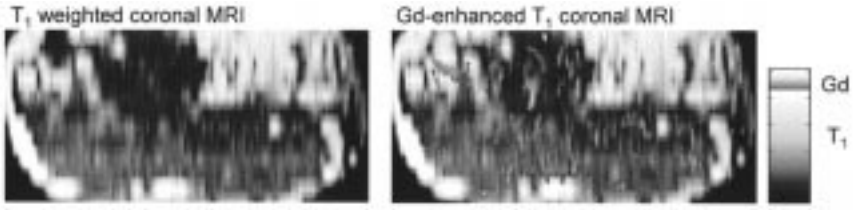

(a) (b)

Fig. 1. (a) T_1-weighted MR coronal slice of a breast. Dark regions indicate parenhymal tissue and light regions indicate adipose tissue. (b) Superposition of the Gd enhancement pattern on the T_1-weighted image in (a). The Gd enhancement is shown according to the colorbar in the right of the image. The Gd-enhancement pattern exhibits a virtually random distribution in the regions of parenhymal tissue and is indicative of breast vascularization.

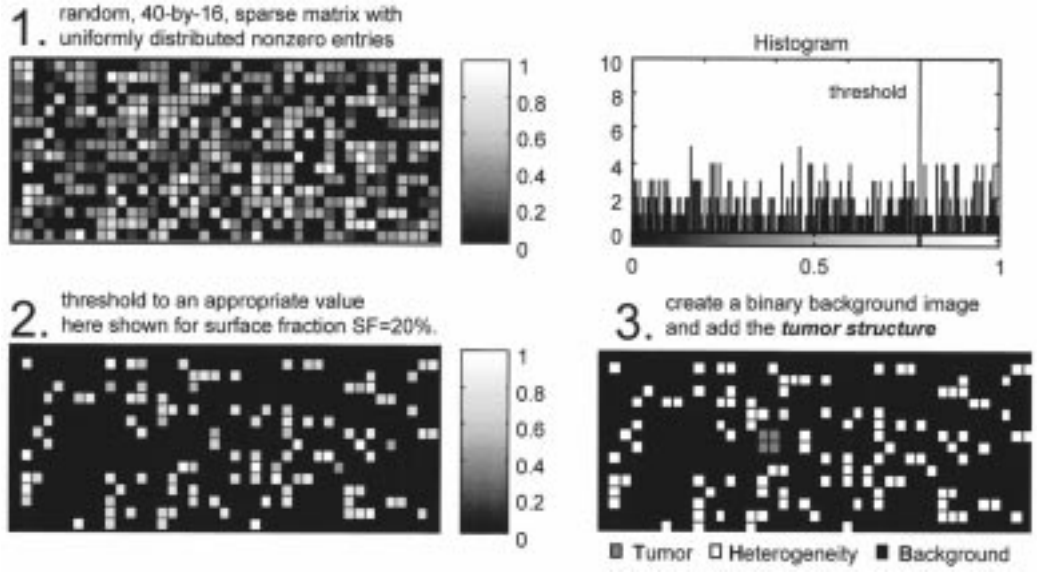

Fig. 2. Steps followed for the creation of the optical property maps used in the simulations. The top right corner image depicts the histogram of the image at step 1.

the appearance of artifacts. The algorithm is found to be virtually independent of the degree of background heterogeneity and a good remedy when *a priori* image information is not available.

II. Research Design and Methods

A. Inhomogeneity Maps

The maps of optical heterogeneity employed have been modeled after Gadolinium (Gd-DTPA) enhanced MR images. Gd-DTPA is a contrast agent that is administered intravenously and delivered via the vascular system. Gd-DTPA rapidly diffuses to the extravascular space [10] after injection. Although an intravascular contrast agent (such as albumin-bound Gd) would indicate vascularization more accurately, the Gd-DTPA enhancement pattern is also indicative of breast vascularization in the general sense, since the agent will distribute at areas with sufficient blood flow and volume. Since vascularization (hemoglobin concentration) is the main intrinsic contrast in breast imaging with light, it may be that breast heterogeneity, especially the absorption contrast, is better modeled using the function-revealing Gd-enhanced images than using the anatomy-revealing T_1-weighted images. Additionally, the Gd-based segmentation better reflects the breast optical heterogeneity expected when NIR contrast agents are injected in the blood stream and for that was selected in this study.

Fig. 1(a) depicts a coronal MR T_1-weighted anatomical image obtained from a 40-year-old patient and Fig. 1(b) depicts the same image superimposed with signal enhancement due to Gd administration. This signal enhancement has been calculated by integrating the Gd contrast over all the coronal slices that covered a volume of thickness ± 0.5 cm above and below the reference T_1-slice seen in Fig. 1(a). Besides a major lesion enhancing at the upper left part of the image (in this case a fibroadenoma) there are patchy enhancements throughout the rest of the image, primarily within the parenchymal tissue regions. The pattern of this enhancement has virtually a random distribution.

In order to model this distribution, we have assumed a random 40×15 matrix with uniformly distributed entries in the range (0 1] as shown in Fig. 2(a). Fig. 2(b) shows the histogram of Fig. 2(a). By applying a threshold we adjusted the degree of heterogeneity of the matrix. Heterogeneity is characterized by the *surface fraction* (SF), i.e.,

$$SF = \frac{\text{number of pixels above threshold}}{\text{total number of pixels}}.$$

For any selected SF, we converted the corresponding matrix to binary and we added a four-pixel rectangular structure, the *tumor* structure, as shown in Fig. 2(d). Therefore, each matrix

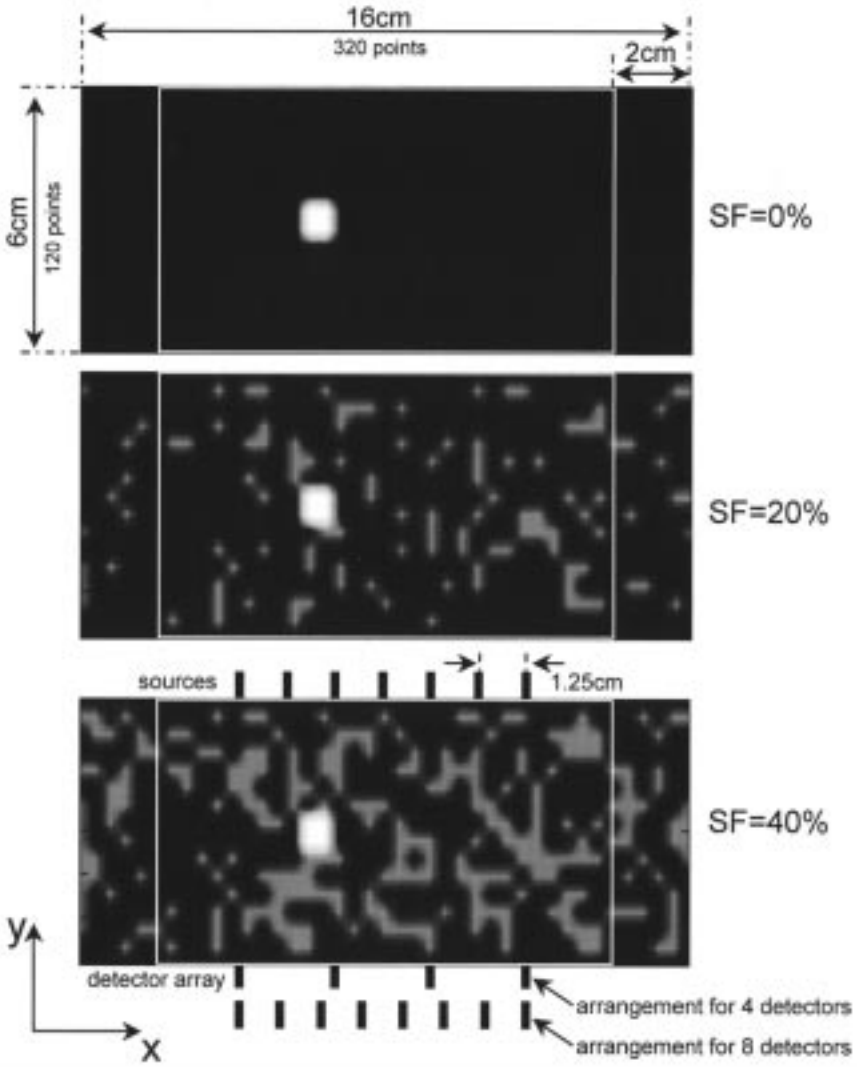

Fig. 3. Optical heterogeneity maps for surface fractions $SF = 0\%$, 20%, and 40%. The thin solid line superimposed on the three maps shown, depicts the ROI that was reconstructed. The geometrical setup used for the simulations is shown in the bottom image, where the sources and the arrangement used for four and eight detectors is also demonstrated.

has three structures: 1) the *background*; 2) the *heterogeneity*; and 3) the *tumor* structure.

B. Optical Property Maps

For creating an optical map, each of the three structures is assigned an absorption coefficient (μ_a) and a reduced scattering coefficient (μ_s') The optical properties assigned were based on the breast optical properties measured with our in-magnet time-resolved optical imager [3]. Each of the resulting 40×15 μ_a and μ_s' optical maps were interpolated to a 320×120 mesh. The final interpolated meshes are shown in Fig. 3 for $SF = 0\%$, 20%, and 40%. The meshes shown were used to create both absorbing and scattering maps. The exact μ_a and μ_s' values assigned are described for each separate study in Section III.

C. Geometrical Setup

The geometry is modeled after our clinical experimental setup[3]. Fig. 3(c) depicts the transmittance geometry assumed, using the optical map produced for $SF = 40\%$. For this study, seven sources and a variable array of detectors (ranging from 4 to 32) in transmission geometry was employed. The span of the detector array is also depicted in Fig. 3. The exact number of detectors employed is explicitly described on a per-case basis in Section III. The region of interest (ROI); namely, the area that is reconstructed in Section III is indicated with a light-solid rectangle.

D. Numerical Solution of the Forward Problem

Each set of μ_a- and μ_s'-maps produced served as an input to a finite-difference implementation of the time-domain diffusion equation. The finite differences problem was solved using an "*alternating directions implicit*" method [8]. The spatial mesh step, was 0.05×0.05 cm^2 and the time resolution of the numerical simulation was 50 ps.

E. Perturbative DOT

The tomographic scheme employed in this study is based on the perturbative solution of the heterogeneous diffusion equation in the frequency domain [11]. Time-domain data are converted to the frequency domain via the Fourier transform,

yielding multiple modulation frequencies. Following the Rytov expansion [11], a measurement at position $\vec{r}_d$, due to a source at position $\vec{r}_s$ can be written as

$$\phi_{\rm sc}(\vec{r}_s,\vec{r}_d,\omega)=\ln\frac{U(\vec{r}_s,\vec{r}_d,\omega)}{U_0(\vec{r}_s,\vec{r}_d,\omega)} \tag{1}$$

where $U(\vec{r}_s,\vec{r}_d,\omega)$ is the photon density (*total field*) of a photon-wave with frequency ω, propagating in the heterogeneous medium, and $U_0(\vec{r}_s,\vec{r}_d,\omega)$, the *incident field*, is the field detected from the same medium if these inhomogeneities were not present. This formulation effectively constitutes a differential measurement [14] since $\phi_{\rm sc}(\vec{r}_s,\vec{r}_d,\omega)$ (the *scattered field*) is the photon field detected only due to the presence of heterogeneities.

The first-order perturbative solution to the heterogeneous equation expresses the scattered field as an integral equation, i.e.,

$$\phi_{\rm sc}(\vec{r}_s,\vec{r}_d,\omega)=\int_V\Big[W^a(\vec{r}_s,\vec{r}_d,\vec{r},\mu_a^0,D^0,\omega)\delta\mu_a(\vec{r}) + W^s(\vec{r}_s,\vec{r}_d,\vec{r},\mu_a^0,D^0,\omega)\delta D(\vec{r})\Big]d\vec{r} \tag{2}$$

where $W^a(W^s)$ represent the absorption (scattering) contributions or weights of perturbations at position $\vec{r}$, due to a source at $\vec{r}_s$ and for a detector at $\vec{r}_d$; μ_a^0, D^0 are the background absorption and diffusion coefficients, respectively, and $\delta\mu_a(\vec{r}),\delta D(\vec{r})$ are the unknown perturbations or variations of the absorption and diffusion coefficient from the background values at position $\vec{r}$. The exact form for the weights is given elsewhere [12],[14]. The transmittance geometry is implemented assuming the method of image sources [13]. For image reconstruction, this integral equation is discretized into a sum of unknown absorption and diffusion coefficients at n discrete positions $\vec{r}_n$ and the scattered field is measured for every source-detector pair and employed frequency ω. For $m=o\times p\times q$ measurements, where o is the number of sources, p is the number of detectors and q is the number of frequencies employed, the discretization yields a set of coupled, linear equations which in matrix form are written as

$$\begin{bmatrix}\phi_{\rm sc}^1(\vec{r}_{s1},\vec{r}_{d1},\omega_1)\\ \vdots\\ \phi_{\rm sc}^m(\vec{r}_{so},\vec{r}_{dp},\omega_q)\end{bmatrix} = \begin{bmatrix}W_{11}^a & \cdots & W_{1n}^a & W_{11}^s & \cdots & W_{1n}^s\\ \vdots & \ddots & \vdots & \vdots & \ddots & \vdots\\ W_{m1}^a & \cdots & W_{mn}^a & W_{m1}^s & \cdots & W_{mn}^s\end{bmatrix}\cdot\begin{bmatrix}\delta\mu_a(\vec{r}_1)\\ \vdots\\ \delta\mu_a(\vec{r}_n)\\ \delta D(\vec{r}_1)\\ \vdots\\ \delta D(\vec{r}_n)\end{bmatrix}. \tag{3}$$

Inverting the weights' matrix determines the spatial map of differences in absorption and diffusion coefficient. For matrix inversion, we have selected the method of projections [11] with relaxation parameter $\lambda=0.1$, applied only on the real part of the weight matrix for simplicity. Convergence was assumed when an additional 100 iterations did not change the result more than 0.1%.

We note that although a two-dimensional (2-D) forward model was used for calculation and demonstration simplicity, the inversion code is by construction 3-D since a volume integral is solved. However, if we assume that all the perturbations lay on the same layer and the rest of the volume considered has no perturbations in it then we can solve a 2-D case with the 3-D inversion code. The mesh size for all inversions was $3\times 3\times 6$ mm^3. The third dimension (6 mm) was selected so that an accurate quantitative reconstruction of the tumor structure was obtained for the absorption map with $SF=0\%$ and was kept constant for all reconstructions.

F. Correction Algorithm

The correction algorithm employed was originally developed for differential measurements of the breast after contrast agent enhancement and has been analytically described [14]. Here, we consider its use in imaging diffuse heterogeneous media using a baseline measurement obtained from a homogeneous "calibration" medium. This approach is suitable for imaging the intrinsic contrast of tissue, namely the absorption and reduced scattering coefficient heterogeneity. The algorithm corrects the scattered field $\phi_{\rm sc}(\vec{r}_s,\vec{r}_d,\omega)$ in (3) to produce the *relative scattered field* $\phi_{\rm sc}^{\rm rel}(\vec{r}_s,\vec{r}_d,\omega)$, i.e.,

$$\phi_{\rm sc}^{\rm rel}(\vec{r}_s,\vec{r}_d,\omega)=\phi_{\rm sc}(\vec{r}_s,\vec{r}_d,\omega)+\ln\frac{U_0^c\left(\vec{r}_s,\vec{r}_d,\omega,\mu_a^{\rm het},\mu_s'^{\rm het}\right)}{U_0^c\left(\vec{r}_s,\vec{r}_d,\omega,\mu_a^{\rm base},\mu_s'^{\rm base}\right)} \tag{4}$$

where $\mu_a^{\rm het},\mu_s'^{\rm het}$ are the average optical properties of the heterogeneous medium, $\mu_a^{\rm base},\mu_s'^{\rm base}$ are the optical properties for $SF=0\%$, and U_0^c is the incident field for transmittance geometry calculated theoretically in the frequency domain using the method of image sources [13]. In practice, U_0^c is the incident field measured experimentally from a calibration medium. For this study, the calibration medium is assumed to have the optical properties of the "background" structure. In real applications, the optical properties $\mu_a^{\rm base},\mu_s'^{\rm base}$ used for the calculation of the relative scattered field in (4) would be the optical properties of the calibration medium.

Using $\phi_{\rm sc}(\vec{r}_s,\vec{r}_d,\omega)$ in (3) reconstructs perturbations from the baseline optical properties. On the other hand, using the $\phi_{\rm sc}^{\rm rel}(\vec{r}_s,\vec{r}_d,\omega)$ in (3) reconstructs the medium relative to its average optical properties. The latter has certain advantages when imaging heterogeneous media as shown in Section III and explained in Section IV. When the $\phi_{\rm sc}^{\rm rel}(\vec{r}_s,\vec{r}_d,\omega)$ is used in (3), the weights $W^a(W^s)$ are also calculated [14] for the medium's average optical properties $\mu_a^{\rm het},\mu_s'^{\rm het}$.

III. Results

This section consists of three parts. Section III-A presents the reconstruction of simulated media with varying degree of background heterogeneity where: 1) only the absorption coefficient was spatially varying; 2) only the reduced scattering coefficient was spatially varying; and 3) both absorption and reduced scattering coefficients were spatially varying. Section

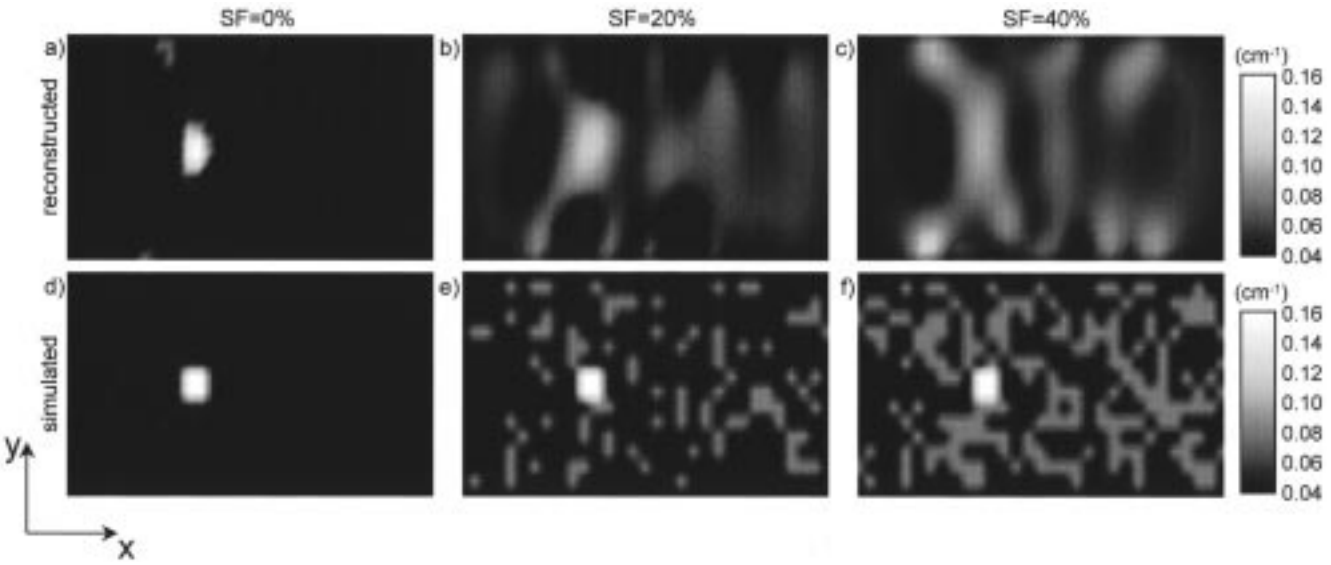

Fig. 4. Reconstruction of absorptive heterogeneity maps as a function of SF. The top row depicts the reconstructed results and the bottom row shows the optical maps simulated. The scattering coefficient is assumed homogeneous and constant at $\mu_s' = 10\ \text{cm}^{-1}$.

III-B shows the reconstruction performance as a function of detectors employed. For simplicity, we have focused only on imaging of absorption perturbations. Section III-C presents imaging improvements when the correction algorithm (4) is applied to the measurement vector. No noise has been added to the measurement vector (besides the numerical simulation approximations) so that the performance of DOT in imaging heterogeneous media is decomposed from its sensitivity to random noise.

A. DOT as a Function of Background Heterogeneity

1) Reconstruction of Absorption: Fig. 4 shows the reconstructed results when only the absorption coefficient was spatially varying, for $SF = 0\%$, 20%, and 40%. The corresponding ROIs, taken from the simulated absorption optical maps, are also shown to facilitate comparison between simulated and reconstructed results. The optical properties used for the simulation are tabulated in Table I. The reconstructions shown employed four detectors spaced 2.5 cm apart and five modulation frequencies (40, 80, 120, 160, and 200 MHz). These results have been produced by inverting (3) without correction. Since scattering was homogeneous the diffusion coefficient perturbations $\delta D(\vec{r}_i), i \in [1 \ldots n]$ in (3) were assumed zero. This simplified the inversion problem by reducing the number of unknowns to half.

Fig. 4(a) shows that when no background heterogeneity was present ($SF = 0\%$), the tumor structure was well resolved. The position was resolved with ~2-mm accuracy, which was the resolution allowed by the reconstruction mesh selected. The size was slightly overestimated, especially along y, which is typical in such transmittance, underdetermined inversions [3]. The reconstruction parameters selected allowed an accurate reconstruction of the magnitude as discussed in Section II. Some minor artifacts appeared close to the borders and can be attributed to numerical and modeling noise.

TABLE I
ABSORPTION HETEROGENEITY

	Tumor	Heterogeneity	Background
μ_a (cm^{-1})	0.16	0.08	0.04
μ_s' (cm^{-1})	10	10	10

Fig. 4(b) and (c) depicts the results for increased surface fraction SF. The tumor structure was resolved with good positional accuracy but its size was significantly overestimated and the magnitude reconstructed was underestimated. The reconstruction errors associated with the tumor structure amplified as the background heterogeneity increased. The background heterogeneity that was reconstructed for surface fractions higher than 0% did not correlate with the simulated background heterogeneity distribution. Distinct "objects" appeared close to the source and detector boundaries. These "objects" or "artifacts" amplified as the background heterogeneity increased [Fig. 4(c)]. The magnitude of the artifacts was comparable or higher than the reconstructed tumor structure, especially for $SF = 40\%$. The position of the artifacts correlated with the position of a source or a detector.

2) Reconstruction of Scattering: Fig. 5 shows the reconstructed results when only the reduced scattering coefficient was spatially varying, for $SF = 0\%$, 20% and 40%. The corresponding ROIs, taken from the simulated scattering optical maps, are also shown. The optical properties used for this simulation are tabulated in Table II. The reconstructions shown employed four detectors spaced 2.5 cm apart and five modulation frequencies (40, 80, 120, 160, and 200 MHz). These results have been produced by inverting (3) without correction. Since the absorption coefficient was constant here, the absorption coefficient perturbations $\delta\mu_a(\vec{r}_i), i \in [1 \ldots n]$

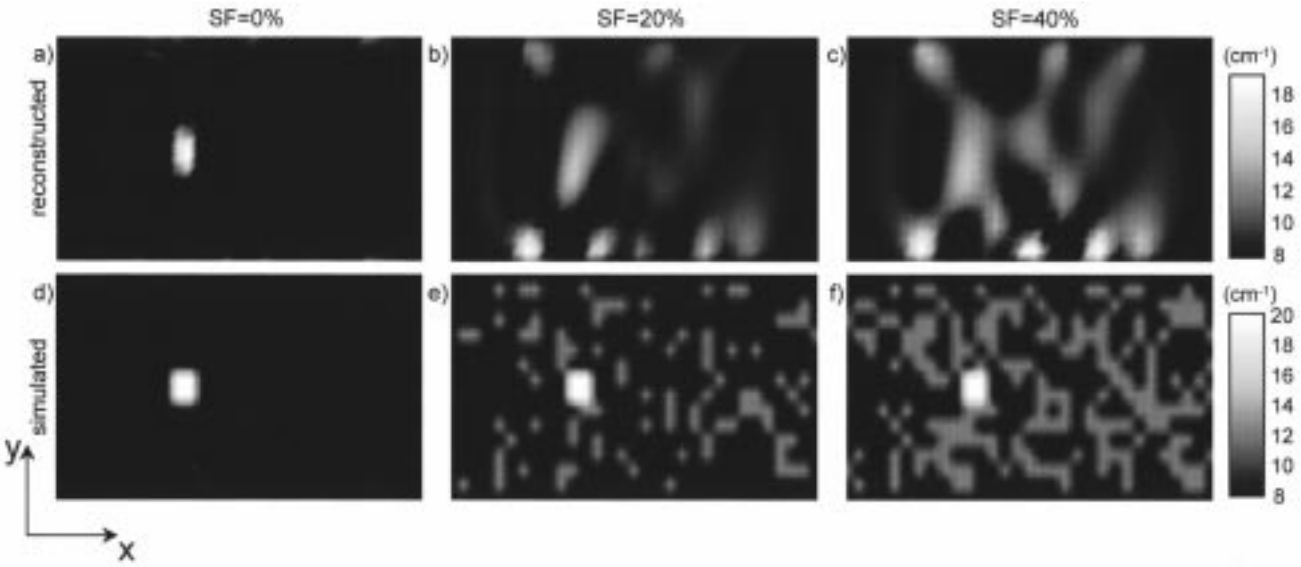

Fig. 5. Reconstruction of scattering heterogeneity maps as a function of SF. The top row depicts the reconstructed results and the bottom row shows the optical maps simulated. The absorption coefficient is assumed homogeneous and constant at $\mu_a = 0.06$ cm^{-1}.

TABLE II
SCATTERING HETEROGENEITY

	Tumor	Heterogeneity	Background
μ_a (cm^{-1})	0.06	0.06	0.06
μ_s' (cm^{-1})	20	12	8

in (3) were assumed zero. This again simplified the inversion problem by reducing the number of unknowns to half.

Fig. 5(a) shows that when no background heterogeneity is present ($SF = 0\%$), the scattering tumor structure was well resolved. Similarly to the absorption reconstructions of Fig. 4 the position of the tumor structure was accurately resolved (within $\sim$2 mm which is the resolution allowed by the reconstruction mesh selected). The size was slightly overestimated along the z axis and is slightly underestimated along the x axis. The magnitude of perturbation is reconstructed with better than 5% error.

As the background heterogeneity increased, the tumor structure was overestimated in size and underestimated in magnitude. The background structures reconstructed appeared "sharper" than the ones seen on the absorption reconstructions (Fig. 4), however, there was again little correlation between reconstructed and simulated background heterogeneity. The appearance of artifacts was stronger here. At $SF = 20\%$, these "boundary" artifacts have already a magnitude higher than the tumor structure. For $SF = 40\%$, more and stronger artifacts appeared.

3) Simultaneous Reconstruction of Absorption and Scattering: Fig. 6 shows results from the reconstruction of simulated media for $SF = 0\%$, 20%, and 40% where both the absorption and the scattering were spatially varying. The absorption and scattering variations had the pattern shown in Fig. 3. The exact optical properties used in the simulation are tabulated in Table III. The reconstructions shown employ again four detectors spaced 2.5 cm. However, since the number of unknowns was doubled from the previous cases, we employed ten modulation frequencies (40–400 MHz in steps of 40 MHz). The reconstruction results shown were again produced by inverting (3) without correction.

The simultaneously reconstructed μ_a and μ_s' images of Fig. 6 are similar to the ones reconstructed independently in Figs. 4 and 5, respectively. The tumor structure was overestimated in size and underestimated in magnitude as the SF increased. Artifacts appeared close to the boundaries as the SF increases. The artifacts appeared stronger on the scattering images.

B. DOT as a Function of Detectors Employed

As seen in Figs. 4–6, imaging fidelity deteriorates as the SF increases. This can be attributed to the fact that an underdetermined problem is inverted. In order to investigate the effect of increased data-set on reconstruction quality, we increased the number of detectors employed to 8, 16, and 32 and reconstructed the absorption heterogeneity map for $SF = 20\%$.

The results are shown in Fig. 7. Fig. 7(a)–(c) depicts the reconstruction results with 8, 16, and 32 detectors, respectively. Fig. 7(d) shows the ROI from the absorption optical map that was simulated. The optical properties are the ones shown in Table I. Fig. 7(e) shows the result of 50 iterative convolutions of the simulated absorption map of Fig. 7(d) with the 3×3 Gaussian kernel shown in Fig. 7(f). This low-resolution image has been provided for comparison reasons.

The increase of the number of detectors resulted in improvements in the reconstruction of the tumor structure. The magnitude of the tumor was more accurately reconstructed as the detector set increased. The size was also more accurately resolved, especially along the x axis but it did not reach the accuracy shown in Fig. 4(a) when no background heterogeneity was present. The background structures were more sharply resolved, but they bear little correlation to the real background heterogeneity distribution [compare to Fig. 7(e)]. The appearance

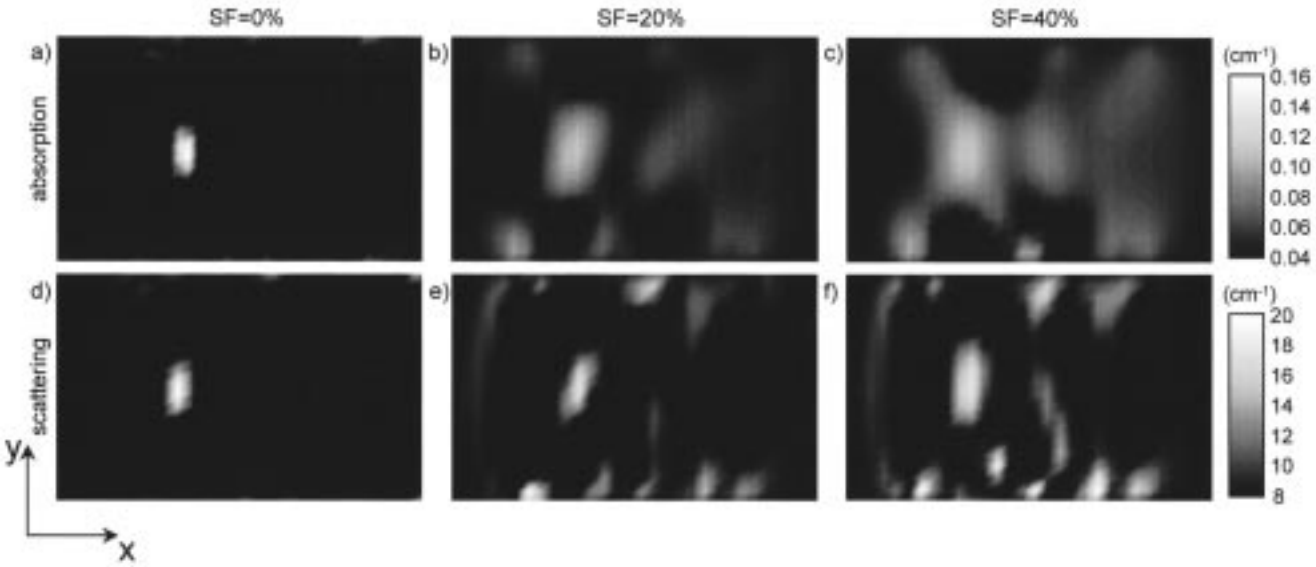

Fig. 6. Simultaneous reconstruction of absorptive and scattering heterogeneity maps as a function of SF. The top row depicts the reconstruction of absorption and the bottom row depicts the reconstuction of scattering. The absorption and scattering optical maps simulated are as shown in Figs. 4 and 5, respectively.

TABLE III
ABSORPTION AND SCATTERING HETEROGENEITY

	Tumor	Heterogeneity	Background
μ_a (cm^{-1})	0.16	0.08	0.04
μ_s' (cm^{-1})	20	12	8

of the characteristic artifacts at the boundaries was reduced but was not eliminated.

C. DOT Using the Correction Algorithm

Fig. 8 shows a comparison between the reconstruction achieved using (3) without correction and the reconstruction achieved when (3) uses the corrected measurement vector [i.e., the relative scattered field in (4)]. The optical properties used for the optical maps are tabulated in Table I. The weights employed when the correction is used are calculated for the average optical properties of the heterogeneous map. For $SF = 20\%$, the average optical properties where $\mu_a^{\text{het}} = 0.048$ cm^{-1}, $\mu_s'^{\text{het}} = 10$ cm^{-1}. For $SF = 40\%$, the average optical properties were $\mu_a^{\text{het}} = 0.056$ cm^{-1}, $\mu_s'^{\text{het}} = 10$ cm^{-1}. The reconstructions shown employ four detectors spaced 2.5 cm apart and five modulation frequencies (40, 80, 120, 160, and 200 MHz).

The correction significantly suppresses the artifacts that appear close to the boundaries. Furthermore, the tumor structure is reconstructed accurately in both size and magnitude. The effect of the correction is that by construction no background structure is reconstructed. This is further explained in Section IV. The algorithm performs well independently of background heterogeneity since the reconstruction results are similar for both $SF = 20\%$ and $SF = 40\%$.

IV. DISCUSSION

DOT can retrieve the location of single objects embedded in *highly heterogeneous* diffuse media when sufficient contrast exists between the object above an average heterogeneous background. However, the reconstruction of size and magnitude becomes less accurate as the background heterogeneity increases. Obviously detection will depend on the size and relative optical property of the object above the average background. In this paper, we focus on the effect of the background heterogeneity to the reconstruction fidelity of the DOT problem and not on "detection limits." Specifically we wanted to demonstrate the presence of strong artifacts in the presence of a distributed heterogeneity and demonstrate a way to improve the reconstructions in that case.

In the presence of background heterogeneity, the single "high-contrast" object will create "correlated" perturbation, i.e., perturbation that is seen in many projections. This correlated perturbation is correctly inverted in the sense that the object is retrieved and accurately localized. On the other hand, the background optical heterogeneity behaves as "biological noise" and appears uncorrelated in the underdetermined system, due to the absence of sufficient independent measurements. The background heterogeneity is detected, since there is contrast reconstructed when the background heterogeneity increases, but it cannot be correctly resolved spatially. The inversion of the underdetermined system, in the presence of the "biological noise," does not converge to an accurate low-resolution spatial map [as would be the one reflected in Fig. 7(e)] but in the reconstruction of artificial structures. The most significant artifacts appear close to the boundaries; preferentially in front of a source or a detector. These artifacts often have much higher contrast than the one expected for the background heterogeneity. Apparently the perturbation obtained from a distributed low contrast inhomogeneity converges erroneously to localized high-contrast objects. Such

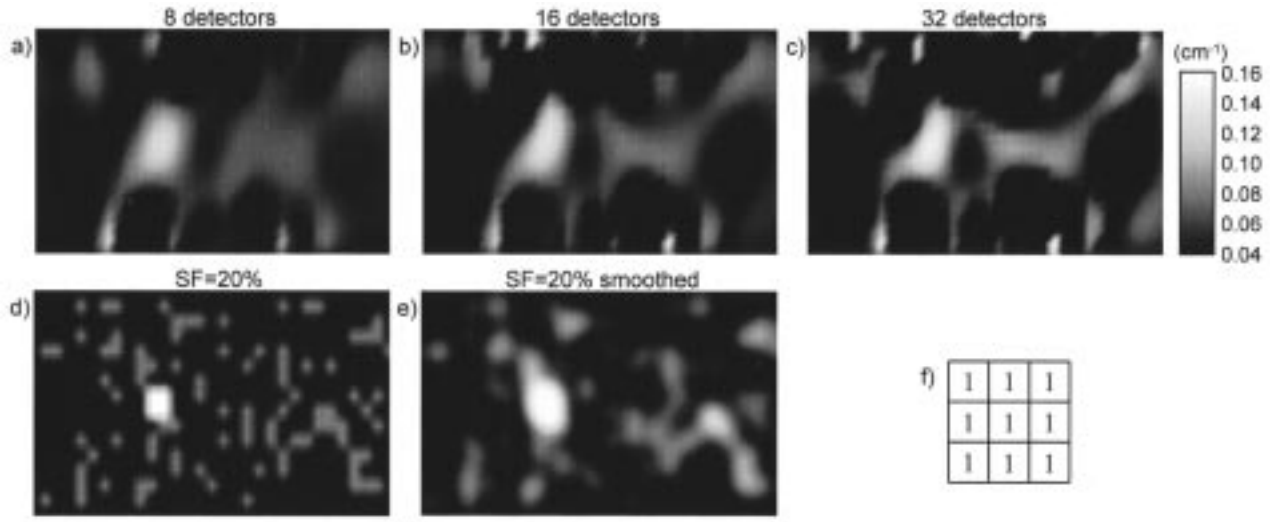

Fig. 7. Reconstruction of absorptive heterogeneity for $SF = 20\%$ as a function of detectors used keeping the number of sources constant. (d) Absorption map simulated. (e) Result of applying the kernel at (f) on image (d) 100 times iteratively to yield a "low resolution" (d) for comparison with the reconstructed results.

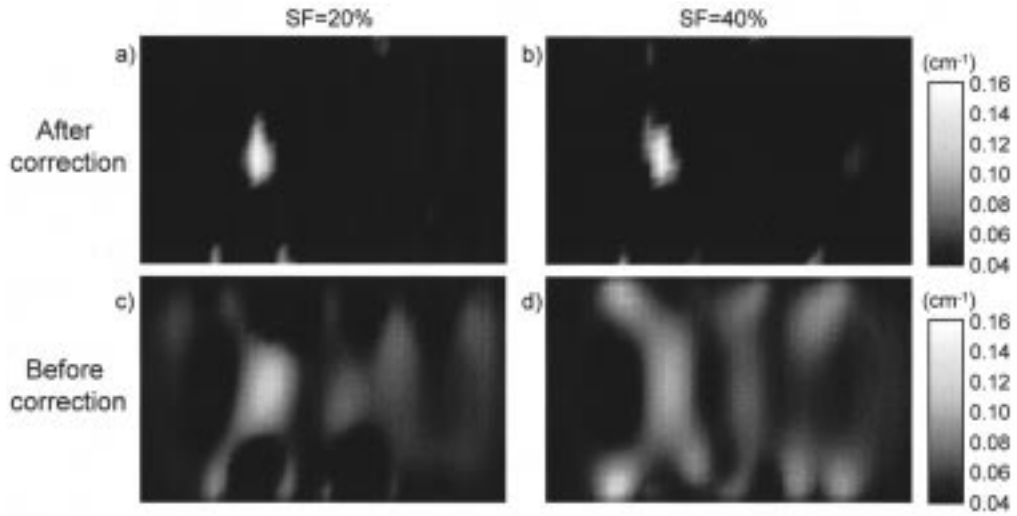

Fig. 8. The effect of the correction algorithm proposed. The top row depicts the reconstruction of absorptive heterogeneity for $SF = 20\%$ and $SF = 40\%$ using the correction algorithm proposed and the bottom row repeats the reconstructions of Fig. 4(e) and (f) where no correction was used.

artifacts have been also seen with other, nonlinear inversion techniques [15] and are not specific to the inversion approach selected here. Generally, a quadrature inversion of underdetermined systems can converge to a solution closest to the initial guess of the minimization [16] (typically, the beginning of axes, i.e., a vector of zeros). Hence the preferential localization of random contrast in front of the sources and detectors satisfies this typical performance. More generally, any uncorrelated information, such as experimental noise, will result in the appearance of artifacts in front of the sources and the detectors. Implementation of more orthogonal measurements (as in the case of a cylindrical geometry or two 90°-rotated transmittance geometries) have been shown to improve imaging of diffuse media systems [17] and may be beneficial to better resolving the background distributed heterogeneity as well, but the same general behavior should be expected in other geometries too, due to the ill-posed nature of the inversion problem.

The correction algorithm proposed offers a practical solution to imaging highly heterogeneous media. This correction assumes that the background heterogeneity contributes to an average absorption and/or scattering increase of the medium. Then it adjusts the measurement vector obtained from an arbitrary baseline (such as a calibration measurement) to an *apparent measurement vector* that corresponds to a measurement from a homogeneous diffuse medium with the average optical properties of the heterogeneous medium measured. The effect of this correction is that it rejects the information that the measurement vector contains on the average absorption increase. Although the "biological noise" is retained its effect diminishes. This results in great artifact suppression. Furthermore the size and magnitude of the tumor structure is more accurately resolved. The algorithm is found to be insensitive to the degree of background heterogeneity and it is expected to work optimally for random heterogeneity distributions as was assumed here. The use of this algorithm has been shown to be beneficial when performing dif-

ferential measurements of tissue such as between the precontrast and postcontrastt enhanced breast [14], [18]. Here, it has been shown that this algorithm could also benefit the reconstruction of objects in highly heterogeneous systems when no *a priori* information is available.

The correction algorithm requires knowledge of the average optical properties of the heterogeneous medium. In this paper, the average optical properties were easily calculated by simple integration over the optical property map. In real measurements, the average optical properties of the medium under investigation can be calculated by fitting the experimental measurements to the appropriate solution of the homogenous diffusion equation for the geometry used. We note that the proposed correction scheme is necessary for noniterative linear techniques, such as the standard perturbation approach employed here. It could be that iterative, nonlinear algorithms that update the optical properties of the reconstructed image automatically account for the difference in bulk optical properties between reference and imaged medium and that this update has effectively a similar mechanism of artifact reduction and image quality improvement. This, however, has to be shown in appropriate studies using iterative algorithms.

Fig. 8 has established that the correction effect is almost independent of the background heterogeneity. Consequently, the practical effect of the correction algorithm is a compensation for the "systematic" change in the average optical properties of the heterogeneous medium; not the exact heterogeneity in terms of random variation. An error in the calculation of background average optical properties will "allow" some of the systematic error to remain in the measurement vector. Therefore, the performance of the correction algorithm using an erroneous estimation of the background optical properties should be similar to the performance of the perturbative method when the background heterogeneity increases, as seen in Figs. 4–7 . For example, the reconstruction of the$SF = 40\%$ medium using a correction scheme that erroneously uses the average optical properties of the $SF = 20\%$ medium (instead of the $SF = 40\%$ medium), would be similar to imaging the $SF = 20\%$ in Section III using no correction.

The tomographic scheme employed in this work was modeled after a clinical implementation of a breast DOT imager [3], [18]. Similarly the media simulated were modeled after the "typical" breast appearance although the anatomy and functional variability of the breast is large. Within these limitations, the results allow insight on the expected performance of the technique in imaging the *in vivo* breast. The conclusions may be extended to other tissue types.

REFERENCES

[1] B. W. Pogue, M. Testorf, T. McBride, U. Osterberg, and K. Paulsen, "Instrumentation and design of a frequency domain diffuse optical tomography imager for breast cancer detection," *Opt. Express*, vol. 1, no. 17, pp. 391–403, 1997.

[2] F. E. W. Schmidt, M. E. Fry, E. M. C. Hillman, J. C. Hebden, and D. T. Delpy, "A 32-channel time-resolved instrument for medical opticaql tomography," *Rev. Sci. Instr.*, vol. 71, no. 1, pp. 256–265, 2000.

[3] V. Ntziachristos, X. H. Ma, and B. Chance, "Time-correlated single photon counting imager for simultaneous magnetic resonance and near-infrared mammography," *Rev. Sci. Instrum.*, vol. 69, no. 12, pp. 4221–4233, 1998.

[4] E. M. Sevick, B. Chance, J. Leigh, S. Nioka, and M. Maris, "Quantitations of time- and frequency- resolved optical spectra for the determination of tissue oxygenation," *Anal. Biochem.*, vol. 195, pp. 330–351, 1991.

[5] B. Beauvoit, T. Kitai, and B. Chance, "Contribution of the mitochondrial compartment to the optical-properties of the rat-liver—a theoretical and practical approach," *Biophys J*, vol. 67, no. 6, pp. 2501–2510, 1994.

[6] J. W. Chang, H. L. Graber, P. C. Koo, R. Aronson, S. L. S. Barbour, and RL. Barbour, "Optical imaging of anatomical maps derived from magnetic resonance images using time-independent optical sources," *IEEE Trans. Med. Imag.*, vol. 16, no. 1, pp. 68–77, Feb. 1997.

[7] B. W. Pogue and K. D. Paulsen, "High-resolution near-infrared tomographic imaging simulations of the rat cranium by use of apriori magnetic resonance imaging structural information," *Opt. Lett.*, vol. 23, no. 21, pp. 1716–1718, 1998.

[8] A. H. Hielscher, A. Klose, D. M. Catarious Jr., and K. M. Hanson, "Tomographic imaging of biological tissue by time-resolved, model-based, iterative, image reconstruction," in *OSA Trends in Optics and Photonics: Advances in Optical Imaging and Photon Migration II*, R. R. Alfano and J. G. Fujimoto, Eds. Washington, DC: Opt. Soc. Amer., 1998, vol. 21, pp. 156–161.

[9] V. Ntziachristos, A. G. Yodh, M. Schnall, and B. Chance, "Comparison between intrinsic and extrinsic contrast for malignancy detection using NIR mammography," in *Optical Tomography and Spectroscopy of Tissue*. San Jose, CA: SPIE, 1999, vol. 3597, pp. 565–570.

[10] R. C. Brasch, H. J. Weinmann, and G. E. Wesbey, "Contrast-enhanced NMR imaging: Animal studies using Gadolinium-DTPA complex," *AJR*, vol. 142, pp. 625–630, 1985.

[11] A. C. Kak and M. Slaney, *Principles of Computerized Tomographic Imaging*. Piscataway, NJ: IEEE Press, 1988, pp. 208–218.

[12] M. A. O'Leary, "Imaging with diffuse photon density waves," masters thesis, Univ. Pennsylvania, Philadelphia, 1996.

[13] P. B. Chance and B. C. Wilson, "Time Resolved Reflectance and Transmittance for the Noninvasive Measurement of Tissue Optical Properties," *J. Appl. Opt.*, vol. 28, pp. 2331–2336, 1989.

[14] V. Ntziachristos, B. Chance, and A. G. Yodh, "Differential diffuse optical tomography," *Opt. Express*, vol. 5, no. 10, pp. 230–242, 1999.

[15] B. W. Pogue, T. O. McBride, J. Prewitt, U. L. Osterberg, and K. D. Paulsen, "Spatially variant regularization improves diffuse optical tomography," *Appl. Opt.*, vol. 38, no. 13, pp. 2950–2961, 1999.

[16] K. Tanabe, "Projection method for solving a singular system," *Numer. Math.*, vol. 17, pp. 203–214, 1971.

[17] B. W. Pogue, T. O. McBride, U. L. Osterberg, and K. D. Paulsen, "Comparison of imaging geometries for diffuse optical tomography of tissue," *Opt. Express*, vol. 4, no. 8, pp. 270–286, 1999.

[18] V. Ntziachristos, A. G. Yodh, M. Schnall, and B. Chance, "Concurrent MRI and diffuse optical tomography of breast after indocyanine green enhancement," *Proc. Nat. Acad. Sci. USA*, vol. 97, no. 6, pp. 2767–2772, 2000.